



**HAL**  
open science

## Multifunctional Amyloid Oligomeric Nanoparticles for Specific Cell Targeting and Drug Delivery

Weiqiang Wang, Rafayel Azizyan, Adriana Garro, Andrey Kajava, Salvador Ventura

► **To cite this version:**

Weiqiang Wang, Rafayel Azizyan, Adriana Garro, Andrey Kajava, Salvador Ventura. Multifunctional Amyloid Oligomeric Nanoparticles for Specific Cell Targeting and Drug Delivery. *Biomacromolecules*, 2020, 21 (10), pp.4302-4312. 10.1021/acs.biomac.0c01103 . hal-03431802

**HAL Id: hal-03431802**

**<https://hal.science/hal-03431802>**

Submitted on 17 Nov 2021

**HAL** is a multi-disciplinary open access archive for the deposit and dissemination of scientific research documents, whether they are published or not. The documents may come from teaching and research institutions in France or abroad, or from public or private research centers.

L'archive ouverte pluridisciplinaire **HAL**, est destinée au dépôt et à la diffusion de documents scientifiques de niveau recherche, publiés ou non, émanant des établissements d'enseignement et de recherche français ou étrangers, des laboratoires publics ou privés.

# Multifunctional Amyloid Oligomeric Nanoparticles for Specific Cell Targeting and Drug Delivery

Weiqiang Wang, Rafayel A. Azizyan, Adriana Garro, Andrey V. Kajava, and Salvador Ventura\*



Cite This: <https://dx.doi.org/10.1021/acs.biomac.0c01103>



Read Online

ACCESS |



Metrics & More

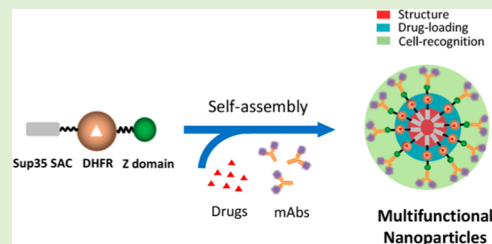


Article Recommendations



Supporting Information

**ABSTRACT:** Natural selection has endorsed proteins with amazing structures and functionalities that cannot be matched by synthetic means, explaining the exponential interest in developing protein-based materials. Protein self-assembly allows fabricating complex supramolecular structures from relatively simple building blocks, a bottom-up strategy naturally employed by amyloid fibrils. However, the design of amyloid-inspired materials with biological activity is inherently difficult. Here, we exploit a modular procedure to generate functional amyloid nanostructures with tight control of their mesoscopic properties. The soft amyloid core of a yeast prion was fused to dihydrofolate reductase through flexible linkers of different sizes. This enabled us to produce, for the first time, biocompatible protein-only amyloid-like oligomeric nanoparticles with defined dimensions in which the embedded enzyme remained highly active, as assessed by biophysical and enzymatic assays. The modular design allowed one to obtain multifunctional nanoparticles by incorporating the antibody-binding Z-domain to the protein fusion. We show how these assemblies can be exploited for antibody-directed targeting of specific cell types and the localized delivery of methotrexate, resulting in the intracellular uptake of the drug by cancer cells and their death. Overall, the novel protein particles we describe in this work might find applications in areas as diverse as biocatalysis, bioimaging, or targeted therapies.



## INTRODUCTION

The design and production of biologically inspired assemblies that can be exploited for the fabrication of functional materials is a rapidly growing area of research.<sup>1</sup> Amyloid fibrils have been traditionally associated with human diseases.<sup>2</sup> However, the recent discovery of amyloids assisting biological functions in a wide range of organisms, from bacteria to humans,<sup>3</sup> has changed this perception and inspired the use of their unique architecture to build up nanostructured materials for applications in biomedicine and biotechnology.<sup>4</sup>

A majority of the available amyloid-based functional nanomaterials result from the self-assembly of short synthetic peptides of natural or artificial origin.<sup>5</sup> In contrast, the assembly of globular proteins into amyloid-like materials with biological activity has been less successful. This is expected since the aggregation of globular domains into amyloid structures necessarily implies a process of conformational conversion in which they lose their native fold and thus their activity.<sup>6</sup>

The main advantage of protein-based materials is the nature of globular proteins, which allows one to alter the material functionality by genetic redesign to fit the intended application. We have recently succeeded in designing highly ordered amyloid-like nanofibrils containing properly folded and highly active proteins using a modular strategy.<sup>7</sup> The distinctive feature of the approach consists in the use of a soft amyloid core (SAC) as the assembling unit. SACs are short amyloidogenic sequence stretches initially identified in the

disordered and low-complexity domains of yeast prions.<sup>8</sup> They differ from the classical amyloid cores of pathogenic proteins in that they are slightly longer and more polar.<sup>9,10</sup> This results in a weaker and more diffuse amyloid propensity but still sufficient to nucleate the self-assembly reaction. The SAC is fused through a Gly/Ser soluble and flexible linker to the globular protein of interest. The resulting fusion proteins are produced recombinantly at high yield and in a soluble manner; still, their ordered aggregation can be induced under defined conditions, rendering functional synthetic amyloid fibrils in which the SAC forms the amyloid spine and the globular domains hang from it in an active conformation, as demonstrated for fluorescent proteins and enzymes.<sup>7</sup>

We use the SAC (residues 100–118) of the Sup35 yeast prion (Sup35-SAC) as the default assembling module. Its small size allows one to use a connecting linker of only eight residues and obtain amyloid fibrils in which the fused protein is active without major steric impediments and with a reduced entropy penalization for the assembly reaction. This is in contrast with natural amyloid proteins displaying a similar architecture, like

Received: July 21, 2020

Revised: September 1, 2020

Published: September 4, 2020

68 the prion proteins Het-s,<sup>11</sup> Sup35p, and Ure2p,<sup>12</sup> human  
69 Rip1/Rip3,<sup>13</sup> or the TAR-DNA binding proteins,<sup>14</sup> where the  
70 connecting linker is significantly longer (>50 residues).

71 Recently, using molecular and mesoscopic modeling, we  
72 were able to establish a theoretical relationship between the  
73 size of a globular domain and the length of the shortest linker  
74 that still allows the formation of infinite amyloid fibrils when  
75 fused to an amyloidogenic sequence.<sup>15</sup> The model suggested  
76 that shortening the linker below this size limit would result in  
77 the formation of oligomers of defined size instead of the typical  
78 fibrils.<sup>16,17</sup> This might provide a unique opportunity to  
79 generate small protein-based nanoparticles decorated with à  
80 *la carte* globular protein functionalities.

81 Here, we connected Sup35-SAC to the dihydrofolate  
82 reductase (DHFR) enzyme<sup>18</sup> (Sup35-DHFR) and demon-  
83 strate that we can control the mesoscopic properties of the  
84 resulting assemblies just by playing with the linker length,  
85 obtaining either catalytic fibrils or catalytic oligomeric  
86 nanoparticles. These nanoparticles are spherical assemblies of  
87 an amyloid-like nature but devoid of any toxicity. They are  
88 homogenous in size, stable, and more active than the  
89 corresponding fibrils.

90 We explored the potential of these novel protein-based  
91 nanoparticles to generate functionalized materials by creating a  
92 tripartite fusion in which we incorporated the Z-domain,<sup>19</sup> an  
93 engineered analog of the B-domain of the *Staphylococcus aureus*  
94 protein A<sup>20</sup> to the C-terminus of the Sup35-DHFR protein.  
95 The new fusion protein also assembles into spherical  
96 oligomeric nanoparticles that can now be decorated with any  
97 antibody of interest, thanks to the Z-domain's nanomolar  
98 affinity for antibodies' Fc domains, thus generating multivalent  
99 particles.

100 We show that antibody-loaded nanoparticles can be directed  
101 specifically against cancer cells and demonstrate that they can  
102 be used as nanocarriers for cell-specific delivery of methotrex-  
103 ate (MTX). MTX acts as an antagonist of folic acid, which is  
104 necessary for DNA synthesis and accordingly is used as a  
105 chemotherapeutic agent for the treatment of cancer.<sup>21,22</sup>  
106 However, it displays a weak pharmacokinetic profile, and  
107 significant off-target toxicity<sup>23–25</sup> and MTX-based nano-  
108 medicines have been designed to overcome these drawbacks.<sup>26</sup>  
109 In our nanoparticles, the Z-domain-bound antibody acts as a  
110 cellular selector and the DHFR moiety as the MTX carrier.  
111 Once released from its carrier, the drug is internalized,  
112 displaying a potent and localized cytotoxic effect. The strategy  
113 is simple and modular and can be adapted to target any cell  
114 type of interest.

## 115 ■ MATERIALS AND METHODS

116 **Reagents and Enzymes.** Reagents and enzymes were purchased  
117 from Sigma-Aldrich (U.K.) unless otherwise stated. Carbon grids  
118 (400 square mesh copper) were purchased from Micro to Nano (The  
119 Netherlands), and the uranyl acetate solution was provided by the  
120 microscopy service at Universitat Autònoma de Barcelona. Sup35-  
121 SAC peptides were purchased from CASLO ApS (Scion Denmark  
122 Technical University).

123 **Expression and Purification of Proteins.** The cDNA of Sup35-  
124 Saa-DHFR, cloned in the plasmid pET28(a) with a His6 tag, was  
125 acquired from GenScript. The constructs pET28(a)/Sup35-8aa-  
126 DHFR, pET28(a)/wild-type DHFR (DHFR-wt), and pET28(a)/  
127 Sup35-Saa-DHFR-Z were obtained by mutagenesis on top of the  
128 plasmid pET28(a)/Sup35-Saa-DHFR. *Escherichia coli* BL21 (DE3)-  
129 competent cells were transformed with the corresponding plasmids.  
130 Then, transformed cells were grown in a 10 mL lysogeny broth (LB)

medium containing 50 µg·mL<sup>-1</sup> kanamycin, overnight at 37 °C and  
transferred into 1 L fresh LB media containing 50 µg·mL<sup>-1</sup>  
kanamycin. After reaching an OD<sub>600</sub> of 0.6, the culture was induced  
with 0.4 mM isopropyl β-D-1-thiogalactopyranoside (IPTG) and  
grown at 20 °C for 16 h. Cells were collected by centrifugation at  
5000 rpm for 15 min at 4 °C. The collected pellet was resuspended  
into 20 mL of phosphate-buffered saline (PBS) pH 7.4 containing 20  
mM imidazole, 1 mg·mL<sup>-1</sup> lysozyme, and 1 mM PMSF. The solution  
was incubated on ice, followed by sonication for 20 min. The  
supernatant was collected by centrifugation at 15 000 rpm for 30 min  
at 4 °C and purified using a nickel-charged IMAC column, followed  
by a gel filtration onto a HiLoad Superdex 75 prep-grade column (GE  
Healthcare). The purified proteins were frozen with liquid nitrogen  
and stored at -80 °C. Sodium dodecyl sulfate-polyacrylamide gel  
electrophoresis (SDS-PAGE) confirmed the purity of the samples.  
The concentrations of the proteins DHFR-wt, Sup35-Saa-DHFR,  
Sup35-8aa-DHFR, and Sup35-Saa-DHFR-Z were determined by  
ultraviolet (UV) absorption using ε values of 33 585, 38 055, 148  
38 055, and 39 420 L·mol<sup>-1</sup>·cm<sup>-1</sup>, respectively.

**Conformational Characterization.** Proteins were dissolved at a  
final concentration of 20 µM in PBS pH 7.4 buffer; then, samples  
were filtered through a 0.22 µm Millipore filter and immediately  
analyzed. Far-UV circular dichroism (CD) spectra were recorded  
from 260 to 200 nm at 1 nm bandwidth, with a response time of 1 s  
and a scan speed of 100 nm·min<sup>-1</sup> in a Jasco-710 spectropolarimeter  
(Jasco Corporation, Japan), thermostated at 25 °C. Ten accumu-  
lations were averaged for each spectrum.

**Aggregation Assay.** Proteins were prepared at 200 µM for  
Sup35-Saa-DHFR and Sup35-8aa-DHFR and at 600 µM for Sup35-  
Saa-DHFR-Z in PBS pH 7.4 and filtered through a 0.22 µm filter. The  
samples were incubated at 25 °C, with agitation for four days. DHFR-  
wt was incubated at the same concentrations and conditions.

**Amyloid Dye Binding.** Thioflavin-T (Th-T) and Congo red  
(CR) were used to monitor the formation of amyloid assemblies. For  
the Th-T binding assay, incubated proteins were diluted to a final  
concentration of 20 µM in PBS pH 7.4, in the presence of 25 µM Th-  
T. Emission fluorescence was recorded in the 460–600 nm range,  
using an excitation wavelength of 445 nm and an emission bandwidth  
of 5 nm on a Jasco FP-8200 spectrofluorometer (Jasco Corporation,  
Japan). For the CR binding assay, incubated proteins were prepared at  
a final concentration of 20 µM and CR was mixed to a final  
concentration of 20 µM. Absorption spectra were recorded in the  
range from 375 to 700 nm in a Specord 200 Plus spectrophotometer  
(Analytik Jena, Germany). Spectra of protein alone and buffer were  
acquired to subtract their contribution to the signal.

**Transmission Electron Microscopy (TEM).** For TEM sample  
preparation, 10 µL of the incubated proteins was deposited on a  
carbon-coated copper grid for 10 min, and the excess liquid was  
removed with filter paper, followed by negative staining with 10 µL of  
2% (w/v) uranyl acetate for 1 min. Grids were scanned using a JEM  
1400 transmission electron microscope (JEOL Ltd., Japan) operating  
at 80 kV, and images were acquired with a CCD GATAN ES1000W  
Erlangshen camera (Gatan Inc.). The particles' diameter was analyzed  
with Image J software (National Health Institute), averaging the  
measures of 100 individual particles.

**Scanning Electron Microscopy (SEM).** A sample of 50 µL of  
incubated protein was centrifuged, and the resulting supernatant was  
removed. The precipitate was resuspended in 50 µL of water and  
washed twice to remove salt traces. Then, 5 µL of the resuspension  
was deposited on a silicon slice (0.5 cm × 0.5 cm) and dried with  
nitrogen flow. Silicon slices were scanned using a Merlin field-  
emission scanning electron microscope (Zeiss Ltd., Germany) at 2  
kV, and images were acquired with an in-lens SE detector. The  
diameter of the particles was calculated with Image J (National Health  
Institute), averaging the measures of 100 individual particles.

**Fourier Transform Infrared (FTIR) Spectroscopy.** DHFR-wt  
was dissolved at 100 µM in PBS, pH 7.4, and filtered through a 0.22  
µm filter. Then, 30 µL of the incubated proteins were centrifuged at  
12 000g for 30 min and resuspended in 10 µL of water. Samples were  
placed on the attenuated total reflectance (ATR) crystal and dried out

201 under a  $N_2$  flow. The experiments were carried out in a Bruker Tensor  
202 27 FTIR (Bruker Optics) supplied with a Specac Golden Gate MKII  
203 ATR accessory. Each spectrum consists of 32 acquisitions measured at  
204 a resolution of  $2\text{ cm}^{-1}$  using the three-term Blackman–Harris  
205 Window apodization function. Data was acquired and normalized  
206 using OPUS MIR Tensor 27 software (Bruker Optics), with the Min/  
207 Max normalization method, which scales spectrum intensities to the  
208 effect that the minimum absorbance unit will be 0 and the maximum  
209 will be 2. Infrared (IR) spectra were fitted employing a nonlinear  
210 peak-fitting equation using Origin 8.5 (OriginLab Corporation).

211 **Fluorescence Microscopy.** First,  $20\ \mu\text{L}$  of incubated fusion  
212 proteins was centrifuged at  $12\ 000g$  for 30 min, and the supernatant  
213 was removed. The precipitate was resuspended in PBS pH 7.4  
214 containing  $100\ \mu\text{M}$  fMTX (methotrexate labeled with fluorescein,  
215 ThermoFisher Scientific) and incubated for 30 min. For the  
216 bifunctional fusion protein Sup35-Saa-DHFR-Z, the precipitate was  
217 resuspended in PBS pH 7.4 containing  $100\ \mu\text{M}$  fMTX and  $1\ \mu\text{g}$  of  
218 anti-EGFR antibody labeled with Alexa 555 (ThermoFisher  
219 Scientific) and incubated for 30 min. Samples were washed three  
220 times to remove any unbound fMTX and antibody and then  
221 resuspended in PBS to a final volume of  $50\ \mu\text{L}$ . Then,  $5\ \mu\text{L}$  of the  
222 resuspension was dropped onto a clean glass slide (Deltalab,  $26\text{ mm} \times$   
223  $76\text{ mm}$ ) and covered by a cover slide (Deltalab,  $22\text{ mm} \times 22\text{ mm}$ ).  
224 Fluorescence imaging of particles and fibrils was carried out on an  
225 Eclipse 90i epifluorescence optical microscope equipped with a Nikon  
226 DXM1200F (Nikon, Japan) camera and ACT-1 software. Images  
227 were acquired with an excitation filter of  $465\text{--}495\text{ nm}$  or  $540\text{--}580$   
228  $\text{nm}$  and detecting fluorescence emission in a range of  $515\text{--}555\text{ nm}$  or  
229  $590\text{--}630\text{ nm}$ .

230 **Dynamic Light Scattering (DLS).** The size of the incubated  
231 proteins was determined using a Malvern Zetasizer Nano ZS90 (ATA  
232 Scientific, Australia) in PBS buffer, pH 7.4, at  $25\ ^\circ\text{C}$ .

233 **Catalytic Activity of Dihydrofolate Reductase Embedded in**  
234 **Amyloid Assemblies.** The Sup35-Saa-DHFR particles and Sup35-  
235 8aa-DHFR fibrils were prepared at  $2\ \mu\text{M}$  in an activity buffer ( $0.1\ \text{M}$   
236 potassium phosphate, pH 7.4,  $1\ \text{mM}$  DTT,  $0.5\ \text{M}$  KCl,  $1\ \text{mM}$   
237 ethylenediaminetetraacetic acid (EDTA),  $20\ \text{mM}$  sodium ascorbate).  
238 Then,  $50\ \mu\text{L}$  of the sample was mixed with  $850\ \mu\text{L}$  of activity buffer in  
239 a cuvette and preincubated at room temperature for 10 min. The  
240 reaction was then initiated by adding  $50\ \mu\text{L}$  of  $2\ \text{mM}$  7,8-  
241 dihydrofolate (DHF) solution and  $50\ \mu\text{L}$  of a  $2\ \text{mM}$  nicotinamide  
242 adenine dinucleotide phosphate (NADPH) solution. Sup35-SAC  
243 fibrils and lysozyme were used as negative controls. For the  
244 determination of the kinetic parameters, a final concentration of  $20$   
245  $\text{nM}$  assemblies and  $20\ \mu\text{M}$  of DHF was preincubated in an activity  
246 buffer at room temperature. The reaction was initiated by adding  
247 NADPH to a final concentration in the range from  $10$  to  $200\ \mu\text{M}$ . The  
248 absorbance change at  $340\ \text{nm}$  was monitored on a Specord 200 Plus  
249 spectrophotometer (Analytik Jena, Germany). The initial velocity at  
250 each concentration was determined upon fitting the reaction with  
251 Origin 8.5 (OriginLab Corporation). The reciprocal of the velocity of  
252 the reaction was plotted against the reciprocal of the concentration of  
253 NADPH. The catalytic constants  $V_{\text{max}}$ ,  $K_m$ ,  $K_{\text{cat}}$ , and  $K_{\text{cat}}/K_m$  were  
254 calculated.

255 **Thermodynamic Dissociation Constants.** The equilibrium  
256 dissociation constants ( $K_d$ ) for enzyme–NADPH complexes were  
257 determined by fluorescence titration at  $25\ ^\circ\text{C}$ . In particular, the  
258 Sup35-Saa-DHFR and Sup35-8aa-DHFR assemblies were prepared at  
259  $100\ \text{nM}$  in an activity buffer in a quartz cuvette. The titrations were  
260 carried out by serial additions of aliquots ( $1\text{--}4\ \mu\text{L}$ ) of NADPH into  
261 the cuvette. The intrinsic fluorescence spectra in the range from  $300$   
262 to  $400\ \text{nm}$  were recorded 2 min after the addition of NADPH, using  
263 an excitation wavelength of  $290\ \text{nm}$  and an emission bandwidth of  $5$   
264  $\text{nm}$  in a Jasco FP-8200 spectrofluorometer (Jasco Corporation,  
265 Japan). A standard tryptophan solution was titrated, and the emission  
266 was used to correct for the inner filter effect caused by NADPH. The  
267 change in intrinsic fluorescence emission at  $340\ \text{nm}$  was plotted  
268 against the NADPH concentration using Origin 8.5 (OriginLab  
269 Corporation), and the  $K_d$  was calculated from the binding equation.

**Preparation of fMTX- or/and Antibody-Loaded Nano-** 270  
**particles.** The incubated protein Sup35-DHFR-Z was precipitated 271  
by centrifugation at  $13\ 000\ \text{rpm}$  for 30 min. The precipitate was 272  
resuspended in PBS buffer pH 7.4 containing  $1\ \mu\text{g}$  of antibody or/and 273  
 $100\ \mu\text{M}$  fMTX (fluorescein-labeled MTX) and then incubated for 30 274  
min. The concentration of nanoparticles was determined by the 275  
reduction of absorbance at  $280\ \text{nm}$  in the supernatant fraction. Three 276  
labeling antibodies (ThermoFisher Scientific)—anti-EGFR antibody 277  
labeled with Alexa fluor 555, anti-CD3 antibody labeled with Alexa 278  
fluor 488, and goat antirabbit antibody labeled with Alexa fluor 555— 279  
were used in this study. Then, the antibody or/and fMTX conjugated 280  
particles were washed three times with PBS buffer to remove any 281  
unbound antibody or/and fMTX and resuspended in PBS buffer. The 282  
antibody-loaded nanoparticles (NPs-anti-EGFR and NPs-anti-CD3), 283  
fMTX-loaded nanoparticles (NPs-fMTX), and fMTX- and antibody- 284  
loaded nanoparticles (NPs-fMTX-anti-EGFR and NPs-fMTX-anti- 285  
rabbit) were used for experiments immediately. 286

**Cell Culture.** The human HeLa and nontumoral lung MRC-5 cell 287  
lines were obtained from the American Type Culture Collection 288  
(ATCC). Both cells were maintained in minimum essential medium  $\alpha$  289  
media (MEM- $\alpha$ ), supplemented with 10% fetal bovine serum (FBS), 290  
and incubated at  $37\ ^\circ\text{C}$  with 5%  $\text{CO}_2$ . 291

**Cytotoxicity Assay.** HeLa and MRC-5 cells were seeded on a 96- 292  
well plate at a concentration of  $3 \times 10^3/\text{well}$  and incubated at  $37\ ^\circ\text{C}$  293  
for 24 h. For HeLa cells, the medium was replaced with  $100\ \mu\text{L}$  of 294  
fresh medium containing the treatments. Unloaded Sup35-Saa- 295  
DHFR-Z particles were assayed in a range of concentrations  $0.5\text{--}$  296  
 $60\ \mu\text{M}$ . MTX-loaded nanoparticles (NPs-MTX), MTX- and anti- 297  
EGFR antibody-loaded nanoparticles (NPs-MTX-anti-EGFR), and 298  
free MTX were assayed in a concentration range of  $2\text{--}20\ \mu\text{M}$ . For 299  
NPs-MTX-anti-EGFR samples, the medium was removed, and cells 300  
were rinsed three times with DPBS buffer after incubation of 20 min. 301  
Then, a fresh medium was added. PBS alone was used as the vehicle 302  
control and the medium without cells as a blank. A final concentration 303  
of  $5\ \text{ng}\cdot\text{mL}^{-1}$  proteinase K was added to the medium to mimic the 304  
proteinase-enriched microenvironment of tumor tissues. For MRC-5 305  
cells, the medium was replaced with a fresh medium containing  $2\text{--}20$  306  
 $\mu\text{M}$  Sup35-Saa-DHFR-Z nanoparticles, followed by addition of 307  
proteinase K to a final concentration of  $5\ \text{ng}\cdot\text{mL}^{-1}$ . Each sample 308  
was measured in triplicate, and the plate was incubated at  $37\ ^\circ\text{C}$  with 309  
5%  $\text{CO}_2$  for 48 h. Then,  $10\ \mu\text{L}$  of the PrestoBlue cell viability reagent 310  
(ThermoFisher Scientific) was added to each well and incubated for 311  
another 1 h. The fluorescence emission was analyzed on a Victor III 312  
Multilabel Plate Reader (Perkin Elmer), equipped with a  $530/10\ \text{nm}$  313  
CW-lamp filter and a  $590/20\ \text{nm}$  emission filter. The viability of cells 314  
was calculated as follows: 315

$$\text{viability (\%)} = (I_{\text{test}} - I_{\text{blank}})/(I_{\text{control}} - I_{\text{blank}}) \times 100\%$$

where  $I_{\text{test}}$ ,  $I_{\text{blank}}$ , and  $I_{\text{control}}$  are the fluorescence intensities of the test, 316  
blank, and control groups, respectively. The significance of the 317  
differences between the test groups and the control was analyzed by 318  
one-way analysis of variance (ANOVA) using the Origin 8.5 program 319  
(OriginLab Corporation). 320

**Confocal Microscopy.** HeLa cells were cultured on an 8-well 321  
Millicell EZ slide (Millipore, Germany) to a final confluence of  $70\text{--}$  322  
 $80\%$ . Then, the medium was replaced with a fresh medium containing 323  
 $20\ \mu\text{M}$  NPs-anti-EGFR and NPs-fMTX-anti-EGFR. The slide was 324  
incubated at  $37\ ^\circ\text{C}$ , 5%  $\text{CO}_2$  for 20 min. The anti-CD3 IgG-loaded 325  
nanoparticles (NPs-anti-CD3) were used as a control. For the 326  
internalization assay, the medium was replaced with a fresh medium 327  
containing  $10\ \mu\text{M}$  Free fMTX and fMTX-loaded nanoparticles (NPs- 328  
fMTX) preincubated with  $50\ \text{ng}\cdot\text{mL}^{-1}$  proteinase for 5 min followed 329  
by addition of EDTA. The slide was incubated at  $37\ ^\circ\text{C}$ , 5%  $\text{CO}_2$  for 4 330  
h. Then, the medium was removed. The adherent cells on the slide 331  
were rinsed three times with a fresh medium. Cells were stained with 332  
CellMask Deep Red (Invitrogen, ThermoFisher Scientific) at a final 333  
dilution of  $1:1000$  for 10 min. The medium was removed and washed 334  
three times with PBS buffer. Cells were fixed with 4% 335  
paraformaldehyde (PFA) at room temperature for 20 min, followed 336  
by a washing step with PBS buffer. Then,  $10\ \mu\text{L}$  of the mounting 337

338 medium containing 4',6-diamidino-2-phenylindole (DAPI) was  
 339 dropped onto each well of the slide and covered with a coverslip.  
 340 The slide was imaged on a Leica TCS SP5 confocal microscope  
 341 (Leica Biosystems, Germany). Images were acquired using 405, 488  
 342 nm, or 561 and 633 nm excitation laser for DAPI, Alexa fluor 488, or  
 343 555 nm and CellMask Deep Red, respectively.

344 **Flow Cytometry Assay.** The NPs-fMTX-anti-EGFR, NPs-fMTX,  
 345 and NPs-fMTX-antirabbit were prepared as described above. HeLa  
 346 cells were prepared in PBS buffer pH 7.4 at a final concentration of  $1$   
 347  $\times 10^6$  mL<sup>-1</sup>. Then, 200  $\mu$ L of HeLa cells was precipitated and  
 348 resuspended in 200  $\mu$ L of PBS buffer containing 20  $\mu$ M NPs-fMTX-  
 349 anti-EGFR, NPs-fMTX, and NPs-fMTX-antirabbit, respectively. After  
 350 30 min of incubation, the cells were pelleted and washed three times.  
 351 Then, 200  $\mu$ L of the cell suspension was analyzed using a  
 352 FACSCalibur cytometer (BD Biosciences, Becton Dickinson),  
 353 equipped with a FITC laser. Fluorescence intensities of cell-bound  
 354 nanoparticles were analyzed and quantitated using FlowJo (BD  
 355 Biosciences). Cells treated with PBS were used as the control.

356 **Proteinase Digestion of fMTX-Loaded Sup35-DHFR-Z**  
 357 **Particles.** The fMTX-loaded particles (NPs-fMTX) were resus-  
 358 pended in PBS buffer containing proteinase K at a final concentration  
 359 of 1  $\mu$ g·mL<sup>-1</sup>. SDS-PAGE was used to analyze the proteolytic progress  
 360 at 15, 30, and 45 min. The supernatant's fluorescence spectrum was  
 361 recorded in the 500–600 nm range at different time points, using an  
 362 excitation wavelength of 488 nm and an emission bandwidth of 5 nm  
 363 on a Jasco FP-8200 spectrofluorometer (Jasco Corporation, Japan).  
 364 The emission maximum was plotted as a function of time. The  
 365 experiment was performed in duplicate. Lysozyme and PBS, instead of  
 366 proteinase K, were used as negative controls.

## 367 ■ RESULTS AND DISCUSSION

368 **Self-Assembly of Sup35-8aa-DHFR into Active Amyloid**  
 369 **Fibrils.** To generate functional amyloid fibrils with a  
 370 previously unexplored catalytic activity, we fused Sup35-SAC  
 371 to the *E. coli* DHFR through an 8-residue-long flexible linker  
 372 consisting of SG<sub>3</sub>SG<sub>2</sub>S (Sup35-8aa-DHFR) (Figure S1A,B).  
 373 The size of DHFR (21.5 kDa) is in the range of GFP (27 kDa)  
 374 and carbonic anhydrase (30 kDa), two proteins that assemble  
 375 into active amyloid fibrils when fused to Sup35-SAC.<sup>7</sup>

376 The fusion protein, Sup35-8aa-DHFR, was expressed  
 377 recombinantly at 64 mg·L<sup>-1</sup> and located in the soluble cellular  
 378 fraction, from which we purified it (Figure S1C). We  
 379 compared the conformational properties of soluble wild-type  
 380 DHFR (DHFR-wt) and Sup35-8aa-DHFR proteins by far-UV  
 381 circular dichroism (CD) (Figure 1A). Their spectra were  
 382 virtually identical, indicating that Sup35-SAC does not induce  
 383 significant changes in the DHFR structure. Then, we used the  
 384 amyloid-specific dyes Thioflavin-T (Th-T) and Congo Red  
 385 (CR) to assess if, despite its solubility, Sup35-8aa-DHFR self-  
 386 assembles with time into amyloid-like structures. To this aim,  
 387 we incubated the fusion protein in PBS buffer pH 7.4 at 37 °C  
 388 for four days. The incubated Sup35-8aa-DHFR protein  
 389 promoted a substantial increase in the Th-T fluorescence  
 390 emission signal, whereas DHFR-wt incubated in the same  
 391 conditions had a negligible effect (Figure 1B). In agreement  
 392 with these results, CR binding was observed for incubated  
 393 Sup35-8aa-DHFR, resulting in a red shift of the CR absorption  
 394 spectrum, while DHFR-wt did not promote any CR spectral  
 395 change (Figure 1C). Moreover, the Fourier transform infrared  
 396 (FTIR) absorbance spectrum of incubated Sup35-8aa-DHFR  
 397 in the amide I region evidenced the existence of a band at 1621  
 398 cm<sup>-1</sup>, which can be assigned to the intermolecular  $\beta$ -sheet  
 399 structure characteristic of amyloids (Figure 1D and Table S1).  
 400 This band was absent in the FTIR spectrum of incubated  
 401 DHFR-wt (Figure S3 and Table S1). The morphological  
 402 analysis of the two protein solutions by negative staining and

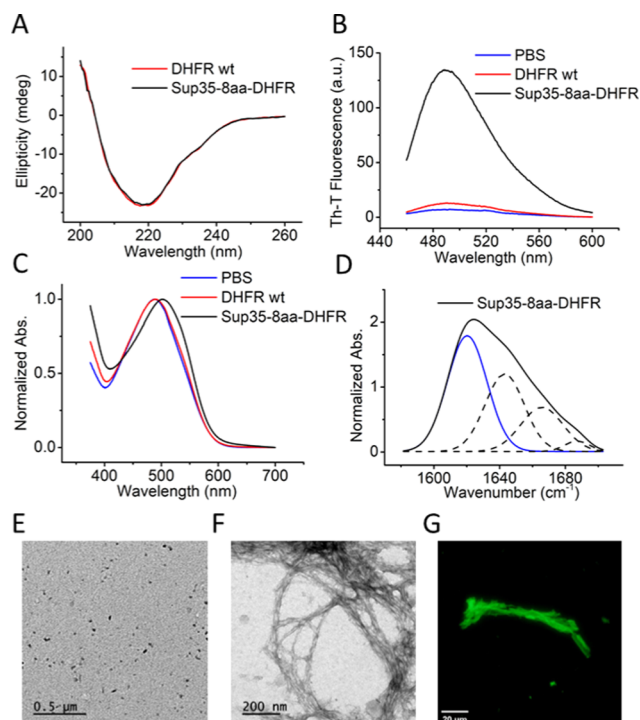


**Figure 1.** Characterization of soluble and aggregated Sup35-8aa-DHFR. (A) Far-UV CD spectra of soluble Sup35-8aa-DHFR and DHFR-wt, shown in black and red, respectively. Incubated Sup35-8aa-DHFR was analyzed by measuring the Th-T fluorescence emission (B) and CR absorbance (C). DHFR-wt and Sup35-8aa-DHFR are shown in red and black, respectively. PBS without protein was included as a control (blue line). (D) FTIR absorbance spectra of incubated Sup35-8aa-DHFR in the amide I region of the spectrum (solid black line) and the component bands (dashed lines); the intermolecular  $\beta$ -sheet component is shown in blue. (E, F) Representative TEM micrographs of incubated proteins upon negative staining: (E) DHFR-wt and (F) Sup35-8aa-DHFR. Scale bar represents 500 and 200 nm, respectively. (G) Fluorescence microscopy image of Sup35-8aa-DHFR fibrils incubated with fMTX. Scale bar represents 20  $\mu$ m.

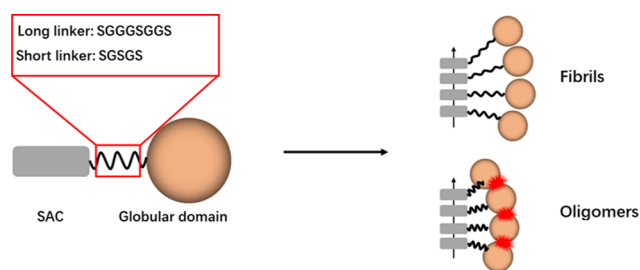


**Figure 2.** Schematic illustration of the rationale for the formation of stable amyloid oligomers. The scheme of SAC (gray box) is connected with a globular domain (orange ball) by linkers of different lengths. Molecules with long linkers can form infinite amyloid fibrils, whereas those with short linkers would form preferably oligomers, owing to the steric restriction imposed by adjacent globular domains.

transmission electron microscopy (TEM) indicated that the  
 403 incubated fusion protein assembled into a typical fibrillar  
 404 amyloid-like structure, whereas DHFR-wt did not form any  
 405 kind of assembly (Figure 1E,F). About  $36.1 \pm 4.2\%$  of the  
 406 original monomer in the solution was incorporated into fibrils  
 407 at the end of the incubation reaction. The average size of the  
 408 fibrils is  $955 \pm 75$  nm, as measured by DLS. This is just a 409

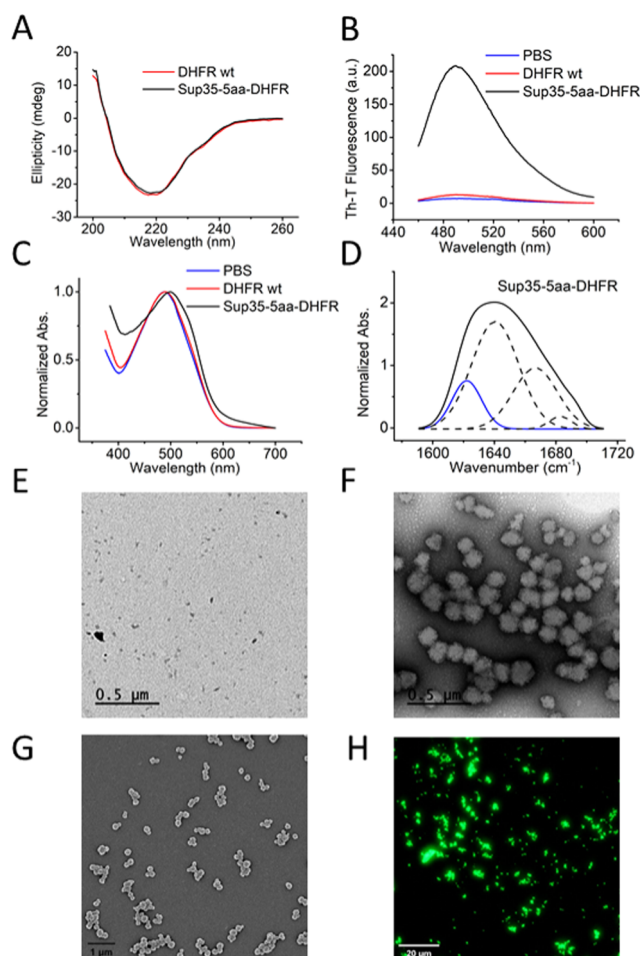


**Figure 3.** Characterization of soluble and aggregated Sup35-5aa-DHFR. (A) Far-UV CD spectra of soluble Sup35-5aa-DHFR and DHFR-wt, shown in black and red, respectively. Incubated Sup35-5aa-DHFR was analyzed by measuring Th-T fluorescence emission (B) and CR absorbance (C). DHFR-wt and Sup35-5aa-DHFR are shown in red and black, respectively. PBS without protein was included as a control (blue line). (D) FTIR absorbance spectra of incubated Sup35-8aa-DHFR in the amide I region of the spectrum (solid black line) and the component bands (dashed lines); the intermolecular  $\beta$ -sheet component is shown in blue. (E, F) Representative TEM micrographs of incubated proteins upon negative staining: (E) DHFR-wt and (F) Sup35-5aa-DHFR. Scale bar represents 500 nm. (G) Representative SEM micrograph of Sup35-5aa-DHFR particles. Scale bar represents 1  $\mu$ m. (H) Fluorescence microscopy image of Sup35-5aa-DHFR particles incubated with fMTX. Scale bar represents 20  $\mu$ m.

410 rough estimation of the fibrils' dimensions, since they are  
411 nonspherical particles.

412 To test if the DHFR enzyme keeps the native structure  
413 within the observed amyloid fibrils, we used a fluorescein-  
414 labeled version of MTX (fMTX), a competitive inhibitor that  
415 binds to the active site of DHFR. In the presence of the  
416 inhibitor, the amyloid fibrils appeared green, as visualized by  
417 fluorescence microscopy (Figure 1G), indicating that fMTX  
418 can bind to the catalytic site of the DHFR moieties embedded  
419 in these nanostructures.

420 **Self-Assembly of Sup35-5aa-DHFR into Amyloid**  
421 **Oligomeric Nanoparticles.** As shown above, a linker of  
422 eight residues suffices to allow the formation of infinite fibrils  
423 in which DHFR remains in its native conformation (Figure 2).  
424 Our recently derived model predicts that introducing a shorter

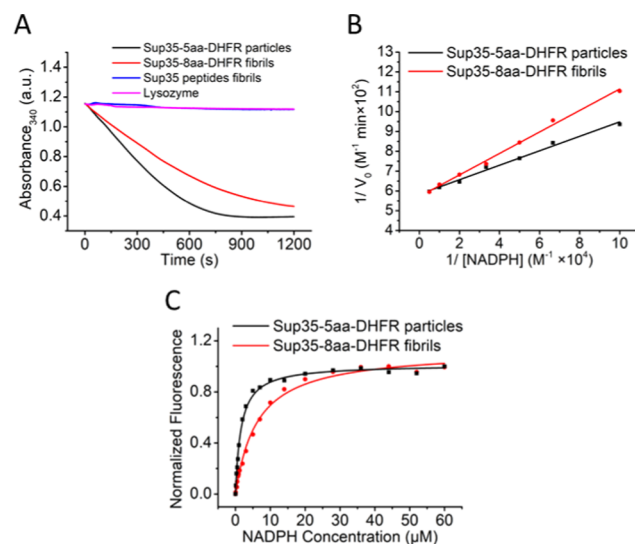


**Figure 4.** Catalytic activity and NADPH binding affinity of Sup35-5aa-DHFR particles and Sup35-8aa-DHFR fibrils. (A) The change in absorbance at 340 nm was monitored for each sample for 20 min in the presence of DHF and NADPH. Both assemblies were prepared at 100 nM. Sup35-SAC peptide fibrils and lysozyme are negative controls. (B) Lineweaver–Burk plot obtained by plotting the reciprocal of initial velocities of reactions against the reciprocal of the concentration of NADPH. (C) Measurement of  $K_d$  for NADPH binding to both assemblies by monitoring the quenching of DHFR intrinsic fluorescence. Fluorescence titrations were performed using 100 nM assemblies and the indicated concentrations of NADPH.

linker to connect the amyloidogenic and globular moieties 425  
would generate steric hindrance and might result in the 426  
formation of oligomeric structures, instead of fibrils (Figure 427  
2).<sup>16</sup> To experimentally demonstrate this hypothesis, we 428  
constructed a Sup35-5aa-DHFR fusion, in which we connected 429  
Sup35-SAC and DHFR with a 5-residue linker consisting of 430  
SGSGS (Figure S2A,B). 431

Again, the protein was well-expressed (71 mg·L<sup>-1</sup>) and 432  
soluble (Figure S2C). Purified Sup35-5aa-DHFR displayed a 433  
conformation very similar to that of DHFR-wt in solution, as 434  
assessed by far-UV CD (Figure 3A). The protein was 435  
incubated at 37 °C for four days, rendering Th-T (Figure 436  
3B) and CR (Figure 3C) positive assemblies, with detectable 437  
intermolecular  $\beta$ -sheet contents (Figure 3D and Table S1). 438  
TEM imaging evidenced that, despite these amyloid-like 439  
properties, and in contrast to Sup35-8aa-DHFR, Sup35-5aa- 440  
DHFR assembles into spherical nanoparticles, which is 441  
consistent with an amyloid oligomeric nature (Figure 3E,F). 442  
The presence of spherical structures in the incubated Sup35- 443  
Saa-DHFR solution was further confirmed by scanning 444  
electron microscopy (SEM) (Figure 3G). About 40.2  $\pm$  445  
3.3% of the original monomer in the solution was incorporated 446  
into nanoparticles at the end of the incubation reaction. 447

The particles were very homogenous in size, with diameters 448  
of 147  $\pm$  20 and 159  $\pm$  24 nm as measured by TEM and SEM, 449  
respectively. These sizes are in good agreement with the 150  $\pm$  450  
50 nm measured for the particles in solution by dynamic light 451  
scattering (DLS) (Figure S4). Incubation of this sample with 452  
fMTX rendered green fluorescent aggregates (Figure 3H), 453  
indicating that, as in the amyloid fibrils, the inhibitor can bind 454  
to folded DHFR domains in the structure of the oligomeric 455  
protein nanoparticles. Therefore, as predicted, playing with the 456  
linker length allowed us to tune the assemblies' mesoscopic 457

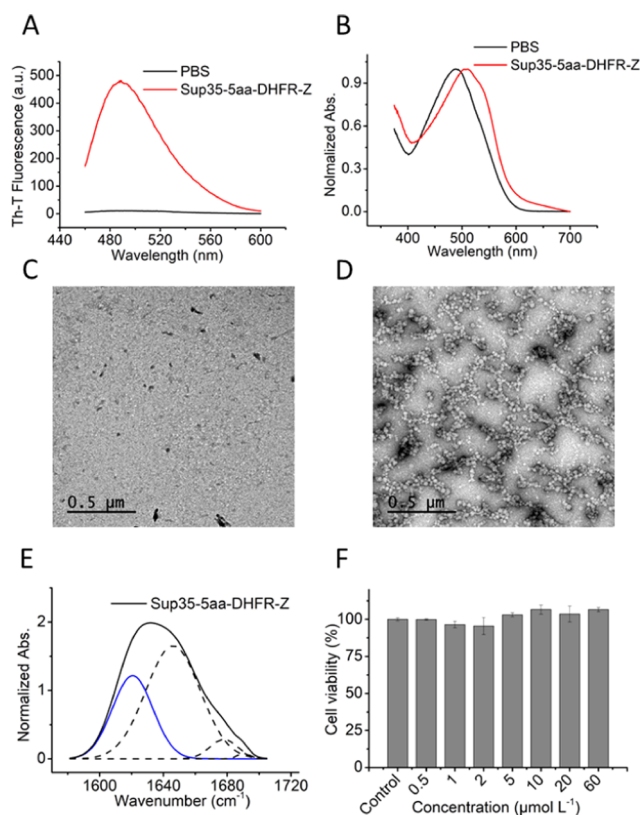


**Figure 5.** Characterization of aggregated Sup35-5aa-DHFR-Z. Incubated Sup35-5aa-DHFR-Z was analyzed by measuring the Th-T fluorescence emission (A) and CR absorbance (B). Sup35-5aa-DHFR-Z is shown in red; PBS without protein was included as a control (black line). Representative TEM micrographs of soluble Sup35-5aa-DHFR-Z (C) and incubated Sup35-5aa-DHFR-Z. (D) Scale bar represents 500 nm. (E) FTIR absorbance spectra of incubated Sup35-5aa-DHFR-Z in the amide I region of the spectrum (solid black line) and the component bands (dashed lines); the intermolecular  $\beta$ -sheet component is shown in blue. (F) Cytotoxicity of incubated Sup35-5aa-DHFR-Z. Results are expressed as means  $\pm$  standard deviation (SD),  $n = 3$ , and analyzed using a one-way ANOVA test. The statistical differences between the control group and the test group were established at  $P < 0.05$ .

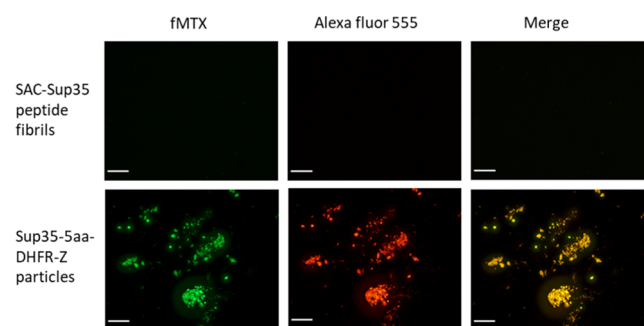


**Figure 6.** Dual-binding activity of Sup35-5aa-DHFR-Z nanoparticles. Representative fluorescence microscopy images of SAC-Sup35 peptide fibrils (upper panel) and Sup35-5aa-DHFR-Z nanoparticles (lower panel) incubated with fMTX (fluorescein, green channel) and an anti-EGFR antibody (Alexa fluor 555, red channel). Scale bar represents 50  $\mu\text{m}$ .

**Catalytic Activity of DHFR in Fibrils and Nanoparticles.** DHFR catalyzes the reduction of dihydrofolate (DHF) to tetrahydrofolate (THF) in the presence of reduced nicotinamide adenine dinucleotide phosphate (NADPH).<sup>27</sup> The binding of fMTX to fibrils and nanoparticles suggested that DHFR might keep its enzymatic activity in both kinds of assemblies. To further confirm this extent and evaluate the impact of each superstructure on the activity of the enzyme, we measured the catalytic activity of fibrils and nanoparticles at 100 nM in the presence of DHF and NADPH. We recorded the absorbance change at 340 nm for 20 min and plotted the resulting traces (Figure 4A). For both fibrils and nanoparticles, the decrease of NADPH absorbance with time indicates that they are catalytically active, whereas the fibrils formed by the Sup35-SAC peptide alone or lysozyme, used as negative controls, do not affect the NADPH absorbance at 340 nm. Importantly, the signal decreased faster for the nanoparticles than for the fibrils, which suggested that the smaller assemblies were more active, assuming that the proportion of properly folded DHFR moieties is similar in both assemblies.

Next, we sought to determine the apparent kinetic constants for both amyloid-like assemblies. We measured the initial velocities of the reactions in the presence of NADPH in a range of concentrations from 10 to 200  $\mu\text{M}$ , while the concentration of DHF was fixed at 20  $\mu\text{M}$ . Then, we calculated the kinetic constants from the resulting Lineweaver–Burk plots (Figure 4B and Table S2). The nanoparticles'  $V_{\text{max}}$  was  $1712 \pm 25 \text{ nM}\cdot\text{min}^{-1}$ , which does not differ significantly from that of the fibrils ( $V_{\text{max}} = 1745 \pm 21 \text{ nM}\cdot\text{min}^{-1}$ ). This was expected since the NADPH binding site and the catalytic center of DHFR should keep the same conformation in both assemblies. However, the nanoparticles exhibited a lower  $K_{\text{m}}$  ( $6.23 \pm 0.32 \mu\text{M}$ ) than that of the fibrils ( $9.44 \pm 0.41 \mu\text{M}$ ). This translates into a higher specificity constant for the nanoparticles ( $K_{\text{cat}}/K_{\text{m}} = 0.23 \pm 0.01 \mu\text{M}^{-1}\cdot\text{s}^{-1}$ ) (Table S2).

The thermodynamic dissociation constants ( $K_{\text{d}}$ ) for binding of NADPH to both assemblies were measured by monitoring the quenching of the DHFR intrinsic fluorescence (Figure 4C). The obtained values indicated that the binding affinity of nanoparticles for NADPH ( $K_{\text{d}} = 1.58 \pm 0.07 \mu\text{M}$ ) was 4-fold higher than that of the fibrils, with a  $K_{\text{d}}$  value of  $6.26 \pm 0.44 \mu\text{M}$  (Table S2). Thus, both the  $K_{\text{m}}$  and  $K_{\text{d}}$  constants indicate that the higher catalytic activity of the nanoparticles results from a higher NADPH binding capability of DHFR when embedded in the spherical amyloid-like structures, likely because the cofactor binding site is more accessible in these assemblies or, alternatively, because the proportion of conformationally active DHFR molecules is higher in the particles than in the fibrils.

Overall, the activity, homogeneity, stability, spherical structure, and moderate size of the novel oligomeric amyloid-like nanoparticles we describe here seem optimal for their exploitation as functionalized nanomaterials.

**Building Up Sup35-5aa-DHFR-Z Bifunctional Nanoparticles.** We sought to exploit the ability of Sup35-5aa-DHFR to form spherical structures of defined size to build up bifunctional nanoparticles with potential applications in targeted delivery. To this aim, we incorporated the Z-domain of *S. aureus* protein A (SpA) at the C-terminus of Sup35-5aa-DHFR through a flexible  $\text{SG}_2\text{SG}$  linker, to obtain the Sup35-5aa-DHFR-Z tripartite fusion protein (Figure 5A,B). The Z-domain is an engineered analog of the B-domain, one of the five homologous IgG-binding domains of SpA.<sup>28</sup> It consists of

458 properties and produce, for the first time, amyloid-like active  
459 spherical nanoparticles.

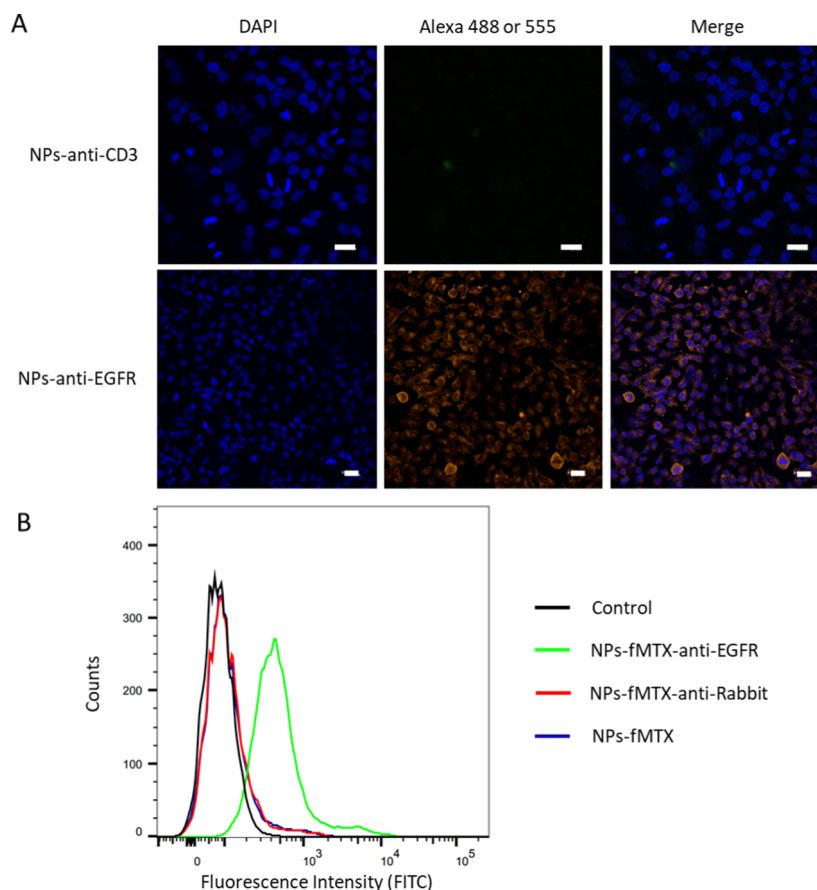


**Figure 7.** Binding specificity of functionalized Sup35-5aa-DHFR-Z nanoparticles to HeLa cells. (A) Representative confocal microscopy images of HeLa cells incubated with nanoparticles conjugated with an anti-CD3 antibody (NPs-anti-CD3, Alexa 488) (upper panel) or an anti-EGFR antibody (NPs-anti-EGFR, Alexa 555) (lower panel). Scale bar represents 20  $\mu\text{m}$ . (B) Quantitative analysis of fluorescein fluorescence on HeLa cells by flow cytometry. HeLa cells were incubated with fMTX, anti-EGFR-loaded nanoparticles (NPs-fMTX-anti-EGFR, green line), fMTX and goat antirabbit antibody-loaded nanoparticles (NPs-fMTX-anti-Rabbit, red line), and fMTX-loaded nanoparticles (NPs-fMTX, blue line). HeLa cells treated with PBS were used as a control. Fluorescein-labeled MTX (fMTX) was used as a fluorescence probe to calculate the proportion of cancer cells bound to nanoparticles using a FITC detector.

523 58 residues (6.5 kDa) and folds into a bundle-like shape  
524 composed of three  $\alpha$ -helices. The Z-domain binds with high  
525 affinity to the Fc region of antibodies from different species  
526 and subclasses. The idea was that if Sup35-5aa-DHFR-Z  
527 assembles into amyloid nanoparticles, we might decorate them  
528 with any antibody of interest.

529 Once more, the protein was well-expressed (80  $\text{mg}\cdot\text{L}^{-1}$ ) and  
530 soluble (Figure S5C). Once purified, we incubated the fusion  
531 protein at 37  $^{\circ}\text{C}$  for four days and assessed whether it binds to  
532 Th-T and CR. Again, the increase in Th-T fluorescence  
533 emission (Figure 5A) and the red shift of the CR absorbance  
534 (Figure 5B) were indicative of an amyloid-like structure. The  
535 band at 1620  $\text{cm}^{-1}$  in the deconvoluted FTIR absorbance  
536 spectra confirmed the presence of the intermolecular  $\beta$ -sheet  
537 structure (Figure 5E and Table S1). Finally, TEM images  
538 showed that Sup35-5aa-DHFR-Z self-assembled into spherical  
539 particles (Figure 5D), whereas the soluble, nonincubated,  
540 tandem fusion protein did not form any assembly (Figure 5C).  
541 The size of such oligomers, as measured by TEM, was  $43.6 \pm$   
542  $2.8$  nm, in good agreement with the  $40.1 \pm 5.8$  nm measured  
543 by DLS. Higher-magnification TEM images showed the high  
544 homogeneity and regular round shape of these nanoparticles  
545 (Figure S6). The size of these nanostructures is  $\sim 1/3$  of that  
546 formed by Sup35-5aa-DHFR. This reduction in size can be  
547 univocally attributed to the presence of the Z-domain. Sup35-

Saa-DHFR-Z is  $\sim 6$  kDa larger than Sup35-5aa-DHFR; thus, if  
548 we assume that the two nanoparticles display similar  
549 compactness, this necessarily implies that the number of  
550 molecules in Sup35-5aa-DHFR-Z particles is significantly  
551 smaller. This reduction in size upon increasing the dimension  
552 of the adjacent domain was already predicted by the above-  
553 described relationship between AR and adjacent globular  
554 domains.<sup>15</sup> The larger the molecule appended to the AR, the  
555 lower the number of units that can be incorporated into the  
556 amyloid-like oligomers, and the smaller the size of the resulting  
557 particle.

**Sup35-5aa-DHFR-Z Bifunctional Nanoparticles are**  
559 **Biocompatible.** One of the main limitations of using  
560 amyloid-like materials in biomedical applications is that they  
561 might possess cytotoxic activity.<sup>29</sup> To discard this possibility,  
562 we tested the cytotoxicity of the Sup35-5aa-DHFR-Z nano-  
563 particles at different concentrations, ranging from 0.5 to 60  
564  $\mu\text{M}$ , using the PrestoBlue assay (Figure 5F). The statistical  
565 analysis using a one-way ANOVA test indicated that the  
566 particles did not exhibit significant toxicity for human HeLa  
567 cells, suggesting that they would have excellent biocompati-  
568 bility.

**Dual-Binding Activity of Sup35-5aa-DHFR-Z Nano-**  
570 **particles.** To confirm that both DHFR and the Z-domain  
571 keep their native structure and functionality in Sup35-5aa-  
572

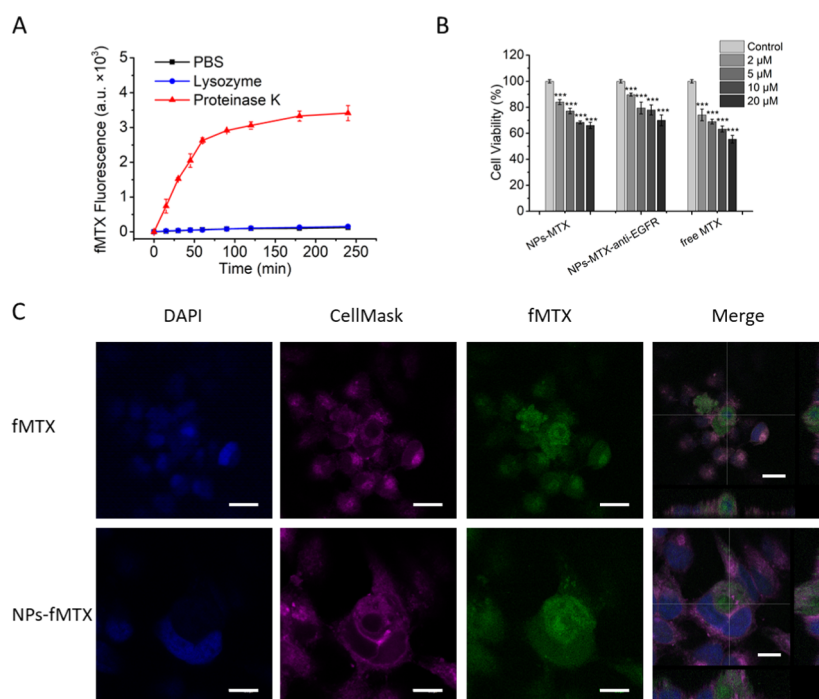


**Figure 8.** Release, uptake, and cytotoxicity of MTX in Sup35-5aa-DHFR-Z nanoparticles. (A) In vitro release of fluorescein-labeled MTX from Sup35-5aa-DHFR-Z nanoparticles in PBS buffer in the presence of  $1 \mu\text{g}\cdot\text{mL}^{-1}$  proteinase K (red line) at  $37^\circ\text{C}$  ( $n = 2$ ). The fluorescence emission of fMTX at 515 nm in the supernatant was measured at the indicated time points. Nanoparticles treated with PBS (black line) and lysozyme (blue line) were used as negative controls. (B) Viability of HeLa cells in the presence of free MTX, MTX-loaded nanoparticles (NPs-MTX), or MTX- and anti-EGFR-loaded nanoparticles (NPs-MTX-anti-EGFR). PBS buffer was used as a control. A final concentration of  $5 \text{ ng}\cdot\text{mL}^{-1}$  proteinase K was added to the medium to mimic the proteinase-enriched microenvironment of tumors. Results are expressed as means  $\pm$  SD ( $n = 3$ ) and analyzed using a one-way ANOVA test. The statistical differences between the control group and the test group were established at  $P < 0.001$ . (C) Representative confocal images of HeLa cells incubated with free fMTX or fMTX-loaded nanoparticles (NPs-fMTX) preincubated with proteinase K. Nuclei were stained with DAPI, and membranes were stained with CellMask Deep Red. Fluorescein-labeled MTX (fMTX) was detected in the FITC channel. Scale bar represents  $10 \mu\text{m}$ .

573 DHFR-Z nanoparticles, we incubated them with fMTX (green  
574 fluorescence) and an anti-EGFR antibody labeled with Alexa  
575 fluor 555 (red fluorescence). Then, they were precipitated and  
576 washed three times to remove any unbound molecule and  
577 resuspended in PBS buffer. When imaged using fluorescence  
578 microscopy, the particles appeared green and red in the  
579 respective channels, and the two signals overlapped when the  
580 channels were merged (Figure 6). This indicated that the  
581 DHFR and the Z-domain embedded in the spherical  
582 nanoparticles were bound to fMTX and the antibody,  
583 respectively. In contrast, the fibrils formed by the SAC-  
584 Sup35 peptide alone did not bind any of the two molecules,  
585 confirming that the observed binding to Sup35-5aa-DHFR-Z  
586 nanoparticles does not result from an unspecific interaction of  
587 the reagents with the common amyloid-like structure.

588 **Sup35-5aa-DHFR-Z-Functionalized Nanoparticles**  
589 **Target Cancer Cells Specifically.** We assessed if Sup35-  
590 Saa-DHFR-Z nanoparticles can target specific antigens in living  
591 cells once they have been loaded with antibodies through their  
592 multiple Z-domains. Nanoparticles loaded with red-labeled  
593 anti-EGFR antibody (NPs-anti-EGFR) were incubated with  
594 HeLa cells, which are known to overexpress EGFR at their  
595 membranes.<sup>30</sup> As can be observed in Figure 7A, confocal  
596 microscopy fluorescence images indicated that the vast  
597 majority of the cells were red fluorescent and, therefore, that  
598 the multivalent NPs-anti-EGFR had recognized them. In  
599 contrast, when the Sup35-5aa-DHFR-Z nanoparticles were  
600 loaded with a green-labeled anti-CD3 antibody and incubated

with HeLa cells, no cellular labeling was detected, consistent  
with the fact that this cell type does not express the CD3  
complex. Thus, the data indicated that the recognition of HeLa  
cells by NPs-anti-EGFR was antibody-driven and specific.

Next, we loaded Sup35-5aa-DHFR-Z nanoparticles, with  
both fMTX and anti-EGFR antibody (NPs-fMTX-anti-EGFR),  
with fMTX and a secondary goat antirabbit antibody (NPs-  
fMTX-antirabbit), or only with fMTX (NPs-fMTX), and we  
added the three functionalized protein nanoparticles to HeLa  
cell cultures. After washing the cells with PBS, they were  
immediately analyzed by flow cytometry, monitoring the green  
fluorescence of fMTX, present in all three nanoparticles, with  
an FITC emission detector. Only HeLa cells treated with NPs-  
fMTX-Anti-EGFR exhibited fMTX fluorescence (Figure 7B),  
whereas no significant fluorescence was detected for HeLa cells  
treated with NPs-fMTX-antirabbit or NPs-fMTX. Flow  
cytometry is quantitative, and the analysis indicated that  
>70% of the cells were bound to NPs-fMTX-anti-EGFR, which  
shows a high binding affinity of the functionalized nano-  
particles for EGFR expressing cells. Indeed, confocal images of  
cells incubated with NPs-fMTX-anti-EGFR indicated that they  
target the cell membrane (Figure S7).

Overall, it appears that Sup35-5aa-DHFR-Z nanoparticles  
provide a modular strategy to target any cell type of interest,  
just by incorporating the adequate antibody thanks to their  
strong interaction with the properly folded Z-domains and the  
multivalency of the assembly.

628 **Proteinase-Controlled Release of MTX from Sup35-**  
 629 **Saa-DHFR-Z Nanoparticles.** Cancer cells secrete a signifi-  
 630 cant number of proteinases, including metalloproteinases,<sup>31</sup>  
 631 serine proteinases,<sup>32</sup> and cathepsins.<sup>33</sup> This feature has been  
 632 exploited to develop proteinase-responsive nanocarriers<sup>34</sup> and  
 633 polymer nanoshells.<sup>35</sup>

634 It is known that amyloid fibrils are highly resistant to  
 635 proteolysis, but we hypothesized that the globular domains  
 636 hanging from the amyloid core in Sup35-Saa-DHFR-Z  
 637 nanoparticles would be protease-sensitive. This will open an  
 638 opportunity to use the DHFR moiety as a carrier for MTX  
 639 under the assumption that the inhibitor will be released from  
 640 the oligomers once they arrive at a protease-rich environment  
 641 and the accessible DHFR domains would be proteolytically  
 642 attacked.

643 We incubated fMTX-loaded nanoparticles with the broad-  
 644 spectrum proteinase K (PK) at a final concentration of 1  $\mu\text{g}\cdot$   
 645  $\text{mL}^{-1}$  and measured the kinetics of fluorescein fluorescence  
 646 apparition in the supernatant, upon centrifugation (Figure 8A).  
 647 The nanoparticles were incubated also in PBS alone or treated  
 648 with lysozyme at the same concentration to ensure that any  
 649 observed release is not spontaneous or unspecific. In contrast  
 650 to control samples, PK-treated nanoparticles showed a  
 651 continuous delivery of fMTX to the solution, with a cumulative  
 652 release efficiency >90% after 4 h of reaction.

653 An SDS-PAGE of the nanoparticles indicated that they were  
 654 SDS-sensitive since, despite high molecular species being  
 655 observed, the vast majority of the fusion protein ran as a  
 656 monomer. This sensitivity to the detergent is typical of  
 657 amyloid oligomers.<sup>36</sup> This allowed us to follow the PK  
 658 digestion by SDS-PAGE, which confirmed that the nano-  
 659 particles are proteinase-sensitive and that no intact Sup35-Saa-  
 660 DHFR-Z fusion remains after 45 min and neither does any  
 661 fragment compatible with an intact DHFR domain (Figure  
 662 S8), explaining why fMTX is released from the protein  
 663 nanoparticles.

664 **Internalization of MTX Released from Loaded Nano-**  
 665 **particles.** We investigated if the DHFR inhibitor released  
 666 from NPs-fMTX can be uptaken by HeLa cells. To this aim,  
 667 we incubated the cells with 10  $\mu\text{M}$  free fMTX or fMTX-loaded  
 668 nanoparticles, both preincubated with 50  $\text{ng}\cdot\text{mL}^{-1}$  PK for 5  
 669 min, followed by protease inactivation with EDTA. After 4 h of  
 670 incubation, the medium was removed, and the cells were  
 671 washed with the medium three times. Then, cells were stained  
 672 with DAPI and CellMask Deep Red for nuclei and membrane  
 673 visualization, respectively. Intracellular green fluorescent fMTX  
 674 was observed by confocal microscopy for both free added  
 675 fMTX and NPs-fMTX (Figure 8C), indicating that the  
 676 nanoparticle-released inhibitor is efficiently internalized.

677 **MTX-Loaded Nanoparticles Induce Death of Cancer**  
 678 **Cells.** We have demonstrated that the MTX-loaded nano-  
 679 particles can liberate DHFR-bound MTX and that the  
 680 inhibitor can internalize into cancer cells. This immediately  
 681 suggested that MTX-loaded nanoparticles could induce  
 682 proteolysis-mediated cell death. Therefore, we measured the  
 683 viability of HeLa cells in the presence of NPs-MTX, NPs-  
 684 MTX-anti-EGFR, or free MTX. A final concentration of 5  $\text{ng}\cdot$   
 685  $\text{mL}^{-1}$  PK was added to the cell culture medium to mimic the  
 686 proteinase-enriched microenvironment of tumor tissues. In all  
 687 cases, a significant dose-dependent decrease in HeLa cell  
 688 viability was observed, compared with control cells incubated  
 689 with PK only (Figure 8B). The concentration of proteinase in  
 690 the assay is lower than the one described in the tumors'

extracellular environment;<sup>37</sup> still, it is sufficient to promote  
 691 MTX release from the nanoparticles, internalization of the  
 692 inhibitor, and cancer cell death. Importantly, untreated and  
 693 PK-treated Sup35-Saa-DHFR-Z nanoparticles are not toxic for  
 694 nontumoral lung MRC-5 cells (Figure S9), indicating that the  
 695 multifunctional nanoparticles might be safe for normal cells in  
 696 vivo. 697

## 698 CONCLUSIONS

In the present work, we first demonstrated that by modulating  
 699 interdomain linker length, one could attain a tight control of 700

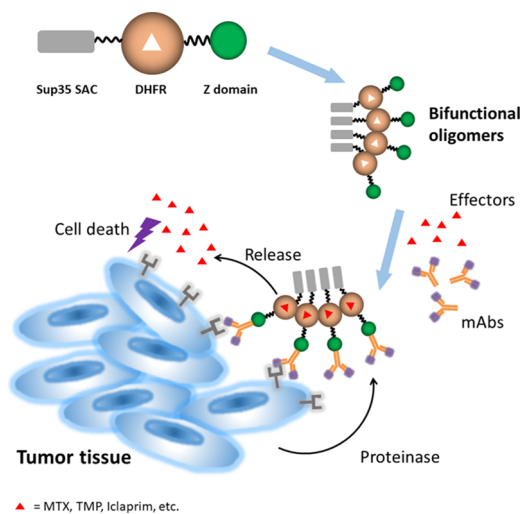


**Figure 9.** Schematic illustration of bifunctional amyloid oligomeric nanoparticles and their potential application for targeted drug delivery. The construct consists of the Sup35 soft amyloid core (Sup35-SAC, gray square), dihydrofolate reductase (DHFR, orange circle), and the Z-domain derived from protein A (green circle). The short linker between Sup35-SAC and DHFR enables the fusion protein to self-assemble into stable bifunctional oligomeric nanoparticles. Drugs (red triangles) and monoclonal antibodies (mAbs) loaded into the nanoparticles would target the tumor cells and release the drugs in a proteinase-enriched environment. As a consequence, the released drugs are internalized and induce the death of the targeted tumor cells.

the mesoscopic properties of the resulting amyloid-like  
 701 nanostructures. This strategy does not require intricate  
 702 structural engineering since it relies on fundamental bio-  
 703 physical principles. The approach allowed us to generate  
 704 oligomeric amyloid-like nanoparticles. These spherical nano-  
 705 particles are homogenous in size, stable, and biocompatible.  
 706 Besides, the multiple globular domains they contain are highly  
 707 active in the assembled state, as shown here for DHFR and the  
 708 Z-domain. Therefore, they constitute a novel kind of functional  
 709 and functionalizable nanomaterial. 710

We provide a proof-of-concept of the utility of these de  
 711 novo-designed nanostructures by showing how they can be  
 712 decorated with an antibody of interest, which act as an  
 713 antenna, directing the multivalent nanoparticles to the specific  
 714 cell types expressing the selected antigen at their surfaces,  
 715 allowing the discrimination between diseased and functional  
 716 cells. When this ability is combined with the capability of  
 717 DHFR to carry and shield MTX, avoiding nonspecific toxic  
 718 effects, it appears as a very appealing strategy for targeted  
 719 delivery of the drug in the proteinase-enriched microenviron-  
 720 ment of tumors, which is followed by MTX internalization into  
 721 9

the cytosol and localized killing of cancer cells (Figure 9). Overall, the multifunctional, self-assembled amyloid nanoparticles we present here constitute a new and safe nanotechnological modular scaffold with the potential of facilitating the specific delivery of agents to specific sites in the body, overpassing the major barrier for bioimaging and tissue-targeted therapies. Importantly, the building blocks of these nanostructures can be produced at high yield and purified at homogeneity from the soluble cell fraction, which results in reduced costs when compared with alternative nanomedicines.

## ASSOCIATED CONTENT

### Supporting Information

The Supporting Information is available free of charge at <https://pubs.acs.org/doi/10.1021/acs.biomac.0c01103>.

Characterization of fusion proteins; FTIR spectrum of DHFR-wt; DLS size distribution of the different assemblies; high-magnification TEM image of Sup35-Saa-DHFR-Z nanoparticles; confocal microscopy images of HeLa cells incubated with nanoparticles; SDS-PAGE analysis of proteinase K digestion; viability of MRC-5 cells; assignment of secondary structure components in the FTIR spectra; kinetics and thermodynamic dissociation constants of the assemblies (PDF)

## AUTHOR INFORMATION

### Corresponding Author

**Salvador Ventura** — Institut de Biotecnologia i Biomedicina and Departament de Bioquímica i Biologia Molecular, Universitat Autònoma de Barcelona, 08193 Bellaterra, Spain; [orcid.org/0000-0002-9652-6351](https://orcid.org/0000-0002-9652-6351); Phone: 34-93-5868956; Email: [salvador.ventura@uab.es](mailto:salvador.ventura@uab.es); Fax: 34-93-5811264

### Authors

**Weiqliang Wang** — Institut de Biotecnologia i Biomedicina and Departament de Bioquímica i Biologia Molecular, Universitat Autònoma de Barcelona, 08193 Bellaterra, Spain;

[orcid.org/0000-0002-6962-8811](https://orcid.org/0000-0002-6962-8811)

**Rafayel A. Azizyan** — Centre de Recherche en Biologie cellulaire de Montpellier, UMR 5237 CNRS, Université Montpellier, Montpellier 34090, France; Institut de Biologie Computationnelle, Université Montpellier, Montpellier 34090, France

**Adriana Garro** — Universidad Nacional de San Luis IMASL-CNICET, San Luis D5702, Argentina

**Andrey V. Kajava** — Centre de Recherche en Biologie cellulaire de Montpellier, UMR 5237 CNRS, Université Montpellier, Montpellier 34090, France; Institut de Biologie Computationnelle, Université Montpellier, Montpellier 34090, France; [orcid.org/0000-0002-2342-6886](https://orcid.org/0000-0002-2342-6886)

Complete contact information is available at:

<https://pubs.acs.org/10.1021/acs.biomac.0c01103>

### Notes

The authors declare no competing financial interest.

## ACKNOWLEDGMENTS

We acknowledge the technical support from the Cell Culture Unit of Servei de Cultius Cel·lulars i Producció d'Anticossos i Citometria (SCAC) and from the Servei de Microscopia of Universitat Autònoma de Barcelona (UAB). This work was funded by the Spanish Ministry of Economy and Competitive-

ness BIO2016-78310-R to S.V. and by ICREA, ICREA-Academia 2015, to S.V. W.W. acknowledges financial support from the China Scholarship Council (CSC): No. 201606500007.

## REFERENCES

- Knowles, T. P.; Mezzenga, R. Amyloid Fibrils as Building Blocks for Natural and Artificial Functional Materials. *Adv. Mater.* **2016**, *28*, 6546–6561.
- Ross, C. A.; Poirier, M. A. Protein Aggregation and Neurodegenerative Disease. *Nat. Med.* **2004**, *10*, S10–S17.
- Fowler, D. M.; Koulov, A. V.; Balch, W. E.; Kelly, J. W. Functional Amyloid—from Bacteria to Humans. *Trends Biochem. Sci.* **2007**, *32*, 217–224.
- Wei, G.; Su, Z.; Reynolds, N. P.; Arosio, P.; Hamley, I. W.; Gazit, E.; Mezzenga, R. Self-Assembling Peptide and Protein Amyloids: from Structure to Tailored Function in Nanotechnology. *Chem. Soc. Rev.* **2017**, *46*, 4661–4708.
- Rufo, C. M.; Moroz, Y. S.; Moroz, O. V.; Stöhr, J.; Smith, T. A.; Hu, X.; DeGrado, W. F.; Korendovych, I. V. Short Peptides Self-Assemble to Produce Catalytic Amyloids. *Nat. Chem.* **2014**, *6*, 303–309.
- Chiti, F.; Dobson, C. M. Protein Misfolding, Amyloid Formation, and Human Disease: A Summary of Progress Over the Last Decade. *Annu. Rev. Biochem.* **2017**, *86*, 27–68.
- Wang, W.; Navarro, S.; Azizyan, R. A.; Baño-Polo, M.; Esperante, S. A.; Kajava, A. V.; Ventura, S. Prion Soft Amyloid Core Driven Self-Assembly of Globular Proteins into Bioactive Nanofibrils. *Nanoscale* **2019**, *11*, 12680–12694.
- Sant'Anna, R.; Fernández, M. R.; Batlle, C.; Navarro, S.; De Groot, N. S.; Serpell, L.; Ventura, S. Characterization of Amyloid Cores in Prion Domains. *Sci. Rep.* **2016**, *6*, No. 34274.
- Sabate, R.; Rousseau, F.; Schymkowitz, J.; Ventura, S. What Makes a Protein Sequence a Prion? *PLoS Comput. Biol.* **2015**, *11*, No. e1004013.
- Sabate, R.; Rousseau, F.; Schymkowitz, J.; Batlle, C.; Ventura, S. Amyloids or Prions? That is the Question. *Prion* **2015**, *9*, 200–206.
- Wasmer, C.; Schütz, A.; Loquet, A.; Buhtz, C.; Greenwald, J.; Riek, R.; Böckmann, A.; Meier, B. H. The Molecular Organization of the Fungal Prion HET-s in its Amyloid Form. *J. Mol. Biol.* **2009**, *394*, 119–127.
- Baxa, U.; Cassese, T.; Kajava, A. V.; Steven, A. C. Structure, Function, and Amyloidogenesis of Fungal Prions: Filament Polymorphism and Prion Variants. *Adv. Protein Chem.* **2006**, *73*, 125–180.
- Li, J.; McQuade, T.; Siemer, A. B.; Napetschnig, J.; Moriwaki, K.; Hsiao, Y.-S.; Damko, E.; Moquin, D.; Walz, T.; McDermott, A.; et al. The RIP1/RIP3 Necrosome Forms a Functional Amyloid Signaling Complex Required for Programmed Necrosis. *Cell* **2012**, *150*, 339–350.
- Chen, A. K.-H.; Lin, R. Y.-Y.; Hsieh, E. Z.-J.; Tu, P.-H.; Chen, R. P.-Y.; Liao, T.-Y.; Chen, W.; Wang, C.-H.; Huang, J. J.-T. Induction of Amyloid Fibrils by the C-terminal Fragments of TDP-43 in Amyotrophic Lateral Sclerosis. *J. Am. Chem. Soc.* **2010**, *132*, 1186–1187.
- Azizyan, R. A.; Garro, A.; Radkova, Z.; Anikeenko, A.; Bakulina, A.; Dumas, C.; Kajava, A. V. Establishment of Constraints on Amyloid Formation Imposed by Steric Exclusion of Globular Domains. *J. Mol. Biol.* **2018**, *430*, 3835–3846.
- Kajava, A. V.; Baxa, U.; Wickner, R. B.; Steven, A. C. A Model for Ure2p Prion Filaments and Other Amyloids: The Parallel Superpleated  $\beta$ -Structure. *Proc. Natl. Acad. Sci. U.S.A.* **2004**, *101*, 7885–7890.
- Azizyan, R. A.; Wang, W.; Anikeenko, A.; Radkova, Z.; Bakulina, A.; Garro, A.; Charlier, L.; Dumas, C.; Ventura, S.; Kajava, A. V. Amyloidogenicity as a Driving Force for the Formation of Functional Oligomers. *J. Struct. Biol.* **2020**, *212*, No. 107604.

844 (18) Schnell, J. R.; Dyson, H. J.; Wright, P. E. Structure, Dynamics,  
845 and Catalytic Function of Dihydrofolate Reductase. *Annu. Rev.*  
846 *Biophys. Biomol. Struct.* **2004**, *33*, 119–140.

847 (19) Tashiro, M.; Tejero, R.; Zimmerman, D. E.; Celda, B.; Nilsson,  
848 B.; Montelione, G. T. High-Resolution Solution NMR Structure of  
849 the Z Domain of Staphylococcal Protein A. *J. Mol. Biol.* **1997**, *272*,  
850 573–590.

851 (20) Forsgren, A.; Sjöquist, J. “Protein A” from *S. aureus*: I. Pseudo-  
852 immune Reaction with Human  $\gamma$ -globulin. *J. Immunol.* **1966**, *97*, 822–  
853 827.

854 (21) Huffman, D. H.; Wan, S. H.; Azarnoff, D. L.; Hoogstraten, B.  
855 Pharmacokinetics of Methotrexate. *Clin. Pharmacol. Ther.* **1973**, *14*,  
856 572–579.

857 (22) Blaney, J. M.; Hansch, C.; Silipo, C.; Vittoria, A. Structure-  
858 Activity Relationships of Dihydrofolate Reductase Inhibitors. *Chem.*  
859 *Rev.* **1984**, *84*, 333–407.

860 (23) Qindeel, M.; Khan, D.; Ahmed, N.; Khan, S.; Rehman, A. U.  
861 Surfactant-Free, Self-Assembled Nanomicelles-Based Transdermal  
862 Hydrogel for Safe and Targeted Delivery of Methotrexate against  
863 Rheumatoid Arthritis. *ACS Nano* **2020**, *14*, 4662–4681.

864 (24) Sadriavadi, K.; Shahbazi, B.; Fattahi, A. De-Esterified  
865 Tragacanth-Chitosan Nano-Hydrogel for Methotrexate Delivery;  
866 Optimization of the Formulation by Taguchi Design. *Artif. Cells,*  
867 *Nanomed., Biotechnol.* **2018**, *46*, 883–893.

868 (25) Tawfik, M. K. Combination of Coenzyme Q10 with  
869 Methotrexate Suppresses Freund’s Complete Adjuvant-Induced  
870 Synovial Inflammation with Reduced Hepatotoxicity in Rats: Effect  
871 on Oxidative Stress and Inflammation. *Int. Immunopharmacol.* **2015**,  
872 *24*, 80–87.

873 (26) Choi, G.; Kim, T.-H.; Oh, J.-M.; Choy, J.-H. Emerging  
874 Nanomaterials with Advanced Drug Delivery Functions; Focused on  
875 Methotrexate Delivery. *Coord. Chem. Rev.* **2018**, *359*, 32–51.

876 (27) Bystroff, C.; Oatley, S. J.; Kraut, J. Crystal structures of  
877 *Escherichia coli* dihydrofolate reductase: The NADP + holoenzyme  
878 and the Folate. cnddot. NADP+ Ternary Complex. Substrate Binding  
879 and a Model for the Transition State. *Biochemistry* **1990**, *29*, 3263–  
880 3277.

881 (28) Moks, T.; ABRAHMSÉN, L.; NILSSON, B.; HELLMAN, U.;  
882 SJÖQUIST, J.; UHLÉN, M. Staphylococcal Protein A Consists of  
883 Five IgG-Binding Domains. *Eur. J. Biochem.* **1986**, *156*, 637–643.

884 (29) Díaz-Caballero, M.; Navarro, S.; Ventura, S. Soluble Assemblies  
885 in the Fibrillation Pathway of Prion-Inspired Artificial Functional  
886 Amyloids are Highly Cytotoxic. *Biomacromolecules* **2020**, *21*, 2334–  
887 2345.

888 (30) Laskin, J. J.; Sandler, A. B. Epidermal Growth Factor Receptor:  
889 A Promising Target in Solid Tumours. *Cancer Treat. Rev.* **2004**, *30*,  
890 1–17.

891 (31) Folgueras, A. R.; Pendas, A. M.; Sanchez, L. M.; Lopez-Otin, C.  
892 Matrix Metalloproteinases in Cancer: From New Functions to  
893 Improved Inhibition Strategies. *Int. J. Dev. Biol.* **2004**, *48*, 411–424.

894 (32) Koshikawa, N.; Yasumitsu, H.; Umeda, M.; Miyazaki, K.  
895 Multiple Secretion of Matrix Serine Proteinases by Human Gastric  
896 Carcinoma Cell Lines. *Cancer Res.* **1992**, *52*, 5046–5053.

897 (33) Koblinski, J. E.; Dosescu, J.; Sameni, M.; Moin, K.; Clark, K.;  
898 Sloane, B. F. Interaction of Human Breast Fibroblasts with Collagen I  
899 Increases Secretion of Procathepsin B. *J. Biol. Chem.* **2002**, *277*,  
900 32220–32227.

901 (34) Zhu, L.; Kate, P.; Torchilin, V. P. Matrix Metalloprotease 2-  
902 Responsive Multifunctional Liposomal Nanocarrier for Enhanced  
903 Tumor Targeting. *ACS Nano* **2012**, *6*, 3491–3498.

904 (35) Yang, J.; Yang, Y.; Kawazoe, N.; Chen, G. Encapsulation of  
905 Individual Living Cells with Enzyme Responsive Polymer Nanoshell.  
906 *Biomaterials* **2019**, *197*, 317–326.

907 (36) Gadad, B. S.; Britton, G. B.; Rao, K. Targeting Oligomers in  
908 Neurodegenerative Disorders: Lessons from  $\alpha$ -Synuclein, Tau, and  
909 Amyloid- $\beta$  Peptide. *J. Alzheimer’s Dis.* **2011**, *24*, 223–232.

910 (37) Schmalfeldt, B.; Prechtel, D.; Härting, K.; Späthe, K.; Rutke, S.;  
911 Konik, E.; Fridman, R.; Berger, U.; Schmitt, M.; Kuhn, W. Increased  
912 Expression of Matrix Metalloproteinases (MMP)-2, MMP-9, and the

Urokinase-type Plasminogen Activator is Associated with Progression 913  
from Benign to Advanced Ovarian Cancer. *Clin. Cancer. Res.* **2001**, *7*, 914  
2396–2404. 915